metals

MDPI

Article

Crystal Chemistry and Electronic Properties of the Al-Rich Compounds, Al_2Cu, ω-Al_7Cu_2Fe and θ-$Al_{13}Fe_4$ with Cu Solution

Changming Fang *, Maaouia Souissi, Zhongping Que and Zhongyun Fan

Brunel Centre for Advanced Solidification Technology (BCAST), Brunel University London, Uxbridge UB8 3PH, UK; maaouia.souissi@brunel.ac.uk (M.S.); zhongping.que@brunel.ac.uk (Z.Q.); zhongyun.fan@brunel.ac.uk (Z.F.)

* Correspondence: changming.fang@brunel.ac.uk

Abstract: In this work, we investigate Cu solution in θ-$Al_{13}Fe_4$ and related Al-rich ω-Al7Cu2Fe and Al_2Cu phases in the Al-Cu-Fe system using the first-principles density functional theory (DFT) with on-site Coulomb interaction correction. The results show preference of Cu at Al_7, forming a ternary θ-$Al_{76}Cu_2Fe_{24}$ at ambient conditions, and both Al_7 and Al_9 sites (in Grin's note), forming θ-($Al_{76}-xCu_2+x$)Fe_{24} at a high temperature. The relative stability of the Al-rich compounds and their crystal and electronic properties are investigated. We show the importance of the Hubbard U correction to the standard DFT functionals for Cu-containing metallic materials. This study helps characterize the intermetallic compounds in Cu-containing Al alloys, and helps further control Fe-containing intermetallic compounds in the solidification of Al-based alloys.

Keywords: Cu solution in θ-$Al_{13}Fe_4$; Cu-containing compounds; crystal chemistry; on-site coulomb correction; density functional theory

Citation: Fang, C.; Souissi, M.; Que, Z.; Fan, Z. Crystal Chemistry and Electronic Properties of the Al-Rich Compounds, Al_2Cu, ω-Al_7Cu_2Fe and θ-$Al_{13}Fe_4$ with Cu Solution. *Metals* **2022**, *12*, 329. https://doi.org/10.3390/met12020329

Academic Editors: Mauro Giovannini and Frank Czerwinski

Received: 14 December 2021
Accepted: 8 February 2022
Published: 13 February 2022

1. Introduction

Fe is the most common impurity in commercial Al metals [1,2]. Due to its low solubility in Al, Fe exists in the form of Fe-containing intermetallic compounds (Fe-IMCs), including the primary θ-$Al_{13}Fe_4$. These Fe-IMCs deteriorate the mechanical performance of cast Al-based parts [1–5]. Al-Cu alloys, including the 2000- and 800-series, have attractive advantages: being light-weight, high strength, and age-hardening. Thus, they have been widely utilized in aerospace and automobile industries [1,5–7]. Information about the Fe-IMCs, including θ-$Al_{13}Fe_4$ and the AlCu precipitates, Al_2Cu and ω-Al_7Cu_2Fe, in the Al-rich part of the Al-Fe-Cu system is of importance to achieve the cast parts of fine microstructure and desirable properties. Moreover, the recycling economy requires that harmful Fe-IMCs, including θ-$Al_{13}Fe_4$, be minimized or at least controlled in the products during the casting of Al alloys, especially Al scrap, which contains various impurities, including Fe [8–10]. In this respect, knowledge about the related compounds/precipitates and Cu solutions in θ-$Al_{13}Fe_4$ is of crucial importance.

Experimental and theoretical efforts have been made on the phase relations in the Al-related compounds and the structures of Fe-IMCs, including θ-$Al_{13}Fe_4$ [1,2,11–33]. Grin and co-workers determined the crystal structure of θ-$Al_{13}Fe_4$ [22] and showed that this compound exhibits rich crystal chemistry. It has a monoclinic lattice (space group C2/m, nr. 12) with lattice parameters, a = 15.492 Å, b = 8.078 Å, and c = 12.471 Å, β = 107.69° [22]. This cell contains 15 Al and 5 Fe species, and 102 atoms in total (78 Al and 24 Fe) (Grin's note) [22]. There is a family of this type of structure, θ-$Al_{13}M_4$ (M = Fe, Co, Ni, and Ru) [23,24]. Moreover, this structure is chemically flexible, and Fe/Al can be partially replaced to form ternary compounds [23,25,26]. As an example, the Cu solution in θ-$Al_{13}Fe_4$ has been under discussion [16–18,25,26]. Freiburg and Grushko investigated the chemical

composition and structural model of θ-$Al_{13}Fe_4$ in the Al-Fe-Cu system and proposed Cu substitution at the Al7 and Al9 sites [25]. Genba and co-workers prepared Al-Fe alloys under Ar protection in a quartz (SiO_2) vessel using pure Al and Fe raw materials [26]. They first heated the sample at 850 °C and then cooled it to 750 °C by quenching it in water. They observed that many needle-like crystals appeared on the surface of the SiO_2 glass tube. Using the X-ray diffraction patterns analysis and electron probe microanalysis, they found Cu at the Fe1, Fe2, Fe3, Al9, Al12, and Al14 sites in θ-$Al_{13}Fe_4$ [26]. First-principles density functional approaches have been applied to investigate the structural, electronic, and magnetic properties of pure θ-$Al_{13}Fe_4$ [23,24,31,32]; its surfaces for catalysis [33,34]; as well as the intrinsic defects in this binary compound [35,36]. Recently, we investigated Si substitution in θ-$Al_{13}Fe_4$ and revealed that Si prefers substitution on two Al sites (Al9 and Al8) in θ-$Al_{13}Fe_4$ [36,37]. Here, we investigate the Cu substitution in θ-$Al_{13}Fe_4$ using a density functional theory (DFT) method with on-site Coulomb interaction correction to Cu 3d electrons. We reveal the preference of Cu at special Al sites, forming $Al_{76}Cu_2Fe_{24}$ at ambient conditions.

The rest of this manuscript is arranged as follows. We first introduce the computational technique and settings in Section 2. Then, we discuss the effect of on-site Coulomb interaction correction on the cohesive properties of the elemental solid Cu and related solids in Section 3.1. This helps us to choose the density functional for future work. The energetics, phase relations, and structural and electronic properties of the Al-rich compounds, θ-$Al_{13}Fe_4$, θ- and θ′-Al_2Cu, and ω-Al_7Cu_2Fe are addressed in Section 3.2. Cu substitution at the atomic sites in θ-$Al_{13}Fe_4$ is described in Section 3.3. We present the crystal structure of the stable θ-$Al_{76}Cu_2Fe_{24}$ in Section 3.4. We compare the theoretical calculations with the experimental observations in Section 4. The results are summarized in Section 5.

2. Methods

We utilized the first-principles' Vienna Ab initio Simulation Package (VASP) [38,39]. This code employs the density functional theory (DFT) within the Projector Augmented Wave (PAW) approach [40]. The spin-polarized Generalized Gradient Approximation (GGA-PBE) [41] was applied for the exchange and correlation energy terms because the GGA approximations describe the 3d metals such as iron, Cu, and related compounds better than the Local Density Approximation (LDA) [42]. We employed a cut-off energy of 550 eV for the wave functions and 700 eV for the augmented wave functions, which better describe the localized 3d electrons of the transition metals. These values are higher than the default values (E_{MMAX}/E_{AUG} = 240.3/291.1 eV for Al, 267.9/511.4 eV for Fe, and 295.4/587.0 eV for Cu). The electronic wave functions were sampled with a dense, 4 × 8 × 6 grid (70–100 ***k***-points) in the irreducible Brillouin zone (BZ) of θ-$Al_{13}Fe_4$ and the related compositions depending on the symmetry, using the Monkhorst–Pack method [43]. First-principles structural optimizations were performed for both lattice parameters and the coordinates of the atoms. Different ***k***-meshes and cut-off energies for the wave functions and augmentation wave functions were tested, which showed suitable convergence (<1 meV per atom).

3. Results

First, we report the calculations for the bulk elemental solids, body-centered cubic (BCC) α-Fe and face-centered cubic (FCC) Al [44], using the DFT-GGA approach with the settings mentioned above. The calculations produced a lattice parameter a = 2.831 Å for ferro-magnetic Fe, and 4.040 Å for Al. The calculated lattice parameters are in agreement with the available experimental values at 0 K, a = 2.8607 Å for Fe and 4.0325 Å for Al [45], as shown in Table 1. The calculations produced a magnetic moment of 2.18 μ_B/Fe, which reproduced the previous results [36,37] and is close to the experimental value 2.10 μ_B/Fe [36,46].

3.1. Effect of on-Site Coulomb Repulsion Correction on Cohesive Properties of Cu

The electron correlation in narrow energy bands was recognized by Hubbard [47]. Based on a Green function technique, Hubbard proposed a simplified model to correct this effect for localized orbitals (Hubbard U) [47]. This approach has been successfully applied to describe, e.g., compounds containing 3d transition metals [48,49]. Recently, we [50] performed calculations using the DFT + U approach and revealed U = 4 eV based on matching the calculated energy position of Cu 3d peak to the photoemission measurements [50,51]. This U value for the occupied Cu 3d electrons is the same as that used in the oxides containing Cu [49] and the systematic study for 3d transition metals using a constrained random-phase approximation [52].

Here, we introduce in detail the cohesive properties of Cu using the standard DFT functionals (LDA and GGA) with/without the Hubbard U (=4 eV) correction. The cohesive energy of an elemental solid is defined as:

$$E_{\mathrm{coh.}} = E(\mathrm{solid}) - E(\mathrm{atom}) \quad (1)$$

Here, E(solid) and E(atom) represent the calculated energies for the solid and isolated atom, respectively. The calculated results are listed in Table 1 compared with selected data from previous calculations and experiments.

One issue to obtain cohesive energy of an elemental solid is the ground state of the individual atom, E(atom) in Equation (1). We performed calculations for the individual atoms with different spin-polarization values in a cube with an axis length of 21 Å. The analyses show that all elemental atoms are spin-polarized and have an integral number of moments: 1 μ_B/atom for Al and Cu, corresponding to their one unpaired 3 s and 4 s electron, respectively (Table 1). Fe atom has a complex electronic configuration with partially occupied 3d orbitals. We performed the atomic energy with different spin-polarization values, including fractional occupations. The results are plotted in Figure 1. An isolated iron atom has an integral spin-polarization number of 4 μ_B/Fe. Based on the calculations, cohesive energies of the elemental solids are obtained according to Equation (1). The available experimental values are included in Table 1 for comparison.

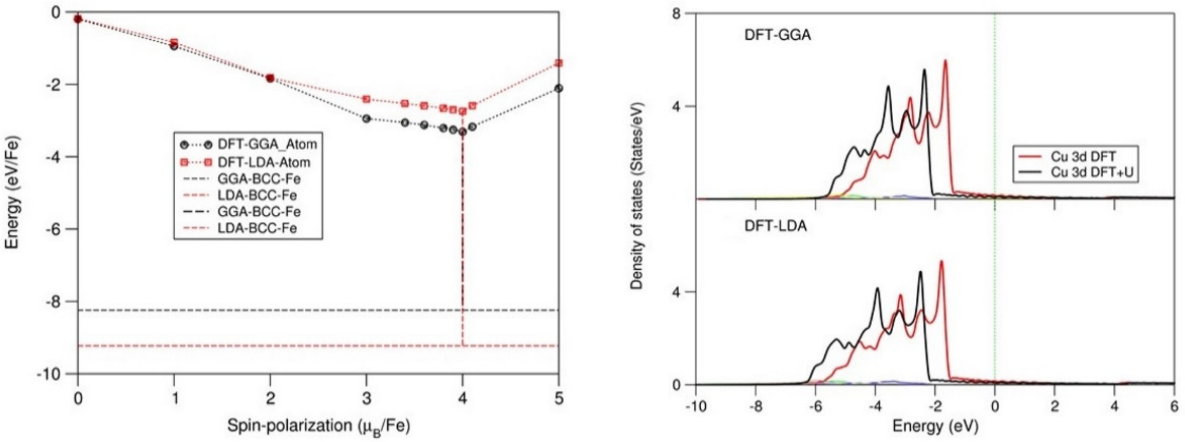

(**a**) (**b**)

Figure 1. (**a**) (Color on line) The calculated energy on magnetic moment for an individual Fe atoms using the standard density functional, LDA and GGA. (**b**) The effect of on-site Coulomb interaction (U = 4 eV) on the Cu 3d states using both GGA (**top**) and LDA (**bottom**).

Table 1 shows the calculated results using different density functionals. The DFT-GGA approximation predicts the lattice parameters of the elemental solids, Al and Fe, with deviations within 1%. Meanwhile, DFT-LDA underestimates the lattice parameters of the elemental solids, especially for iron. Moreover, the estimated cohesive energies of the elemental solids from the DFT-GGA are in much better agreement with the available

experimental values in the literature than those from the DFT-LDA, which agrees with the previous work that DFT-GGA works better for solids, especially for transition metals and their compounds [41,42].

Table 1. Calculated cohesive properties (lattice parameter, cohesive energy) for elemental solids Al, Fe, and Cu using both DFT and DFT+ U methods (U = 4 eV) with comparison with available experimental values and previous calculations in the literature.

Property	LDA	LDA + U	GGA	GGA + U	Exper. (0 K)
Al: Face-Centered Cubic (FCC) lattice. Electronic configuration, [Ne] $3s^2$ $3p^1$					
a (Å)	3.984 (−1.2%)	-	4.039 (+0.2%)	-	4.0325 [45]
E_{coh} (eV/Al)	−4.020 (+15.7%)	-	−3.511 (+3.6%)	-	−3.39 [46,53]
α-Fe: Body-Centered Cubic (BCC) lattice. Electronic configuration, [Ar] $3d^6$ $4s^2$					
a (Å)	2.747 (−4.0%)	-	2.831 (−1.0%)	-	2.8607 [45]
E_{coh} (eV/Fe)	−6.480 (+51.4%)	-	−4.933 (+15.3%)	-	−4.28 [46]
Cu: Face-Centered Cubic (FCC) lattice. Electronic configuration, [Ar] $3d^{10}$ $4s^1$					
a (Å)	3.523 (−2.2%) 3.553 (−1.4%) [46]	3.496 (−2.9%)	3.635 (+0.9%) 3.630 (+0.7%) [30] 3.676 (+2.0%) [46]	3.622 (+0.6%)	3.6032 [45]
E_{coh} (eV/Cu)	−4.676 (+34.4%) −4.353 [46]	−4.288 (+23.2%)	−3.501 (+0.6) −3.48 [30]	−3.079 (−11.5%)	−3.48 [30] −3.524 [54]
E (3d) (eV)	−1.78	−2.49	−1.65	−2.34	−2.4 (UPS) [51] −3.2 (XPS) [51]

Calculations using both LDA and LDA + U approaches markedly underestimate the lattice parameter of Cu (over 2%) (Table 1). Moreover, the calculated cohesive energies are notably higher than the experimental values. The DFT-GGA calculations produced lattice parameters in agreement with the experimental value (deviation of 0.9%), and the GGA + U calculations resulted in an even better agreement with the experiment (0.6%). The value of the cohesive energy from GGA using the current settings is slightly higher than the experimental values (~4%). The GGA + U calculations produced cohesive energy of about −3.078 eV/Cu in Al, which is notably smaller than the GGA calculations. The experimental values are in between the GGA and the GGA + U calculations. However, this GGA + U value is close to the value −3.046 eV/Cu from the advanced hybrid functional approach [30,55,56]. This is understandable, that the GGA + U approximation corrects the unphysical interaction between the 3d electrons and the neighboring Cu atoms, similar to that in the advanced hybrid functionals [55,56]. This result also indicates that Cu 3d electrons are better treated as a semi-core level.

The Hubbard U correction puts the Cu 3d states about 0.7 eV lower in energy for both LDA(+U) and GGA(+U) methods (Table 1 and Figure 1b), in agreement with the recent study [50]. The peak of the Cu 3d states is about 2.3 eV below the Fermi level, close to the experimental value from ultra-violet photoelectron spectrum (UPS) observations (2.4 eV) [51].

Overall, the DFT-GGA predicts the cohesive properties of the elemental solids, especially the 3d transition metals, notably better than the DFT-LDA. The Hubbard U approach corrects the unphysical interaction of the Cu 3d electrons with the neighboring atoms and thus produces less cohesive energy. In the rest of this work, we only use the DFT + GGA with the Hubbard U correction for the Cu-containing compounds.

3.2. The Al-Rich Compounds θ-$Al_{13}Fe_4$, Al_2Cu, and ω-Al_7Cu_2Fe in the Al-Fe-Cu System

The formation energy of, e.g., a ternary compound $A_lB_mC_n$ with respect to the elemental solids A, B, and C is defined as,

$$\Delta E(A_lB_mC_n) = E(A_lB_mC_n) - [l\ E(A) + m\ E(B) + n\ E(C)] \quad (2)$$

where $E(A_lB_mC_n)$ and E(A), E(B), and E(C) are the calculated total-electron energies for $A_lB_mC_n$ and the elemental solids A, B, and C, respectively.

The computed results (lattice parameters and formation energies) for the Al-rich compounds in the Al-Cu-Fe system are listed in Table 2. Available experimental results are included for the sake of comparison. The schematical structures and related coordination of the transition metals are shown in Figure 2.

The calculated lattice parameters for the compounds are in agreement with the available experimental data within 1%, except for the a-axis of θ′-Al_2Cu, the calculated value of which is about 1.3% greater than the experimental data.

Table 2. Calculated results (lattice parameters, formation energies according to Equation (2)) for the stable structure in the binary and ternary systems at ambient conditions. Experimental data in the literature are included for comparison.

Compounds	Calculated Latt. Para. (Å)/Form. Energy		Experiments
	GGA	GGA + U	
θ-$Al_{13}Fe_4$, Mon. C2/m, (nr. 12)	a = 15.426 b = 8.022 c = 12.425 β = 107.68 (°) V = 1464.92 (Å^3/cell) ΔE_{form} = −0.329 eV/atom		a = 15.492 b = 8.078; c = 12.471 β = 107.69(°); V = 1486.88(Å^3/cell) [22] ΔE_{form} = −0.225 to −0.310 eV/atom [38–40]
θ-Al_2Cu, Tetr. I4/mcm (Nr.140)	a = 6.066 c = 4.874 V = 179.36 ΔE_{form} = −0.157	6.064 4.864 178.88(Å^3/cell) −0.125(eV/atom)	a = 6.054 [57]; 6.063 [58];6.067 [59,60] c = 4.864 [57]; 4.872 [58]; 4.877 [59,60] V = 178.27 (Å^3/cell) [57],179.09 [58],179.52 [59,60]
θ′-Al_2Cu, Tetr. I-4m2 (Nr.119)	a = 4.093 c = 5.786 V = 96.94 ΔE_{form} = −0.176	4.092 5.782 96.81(Å^3/cell) −0.124 (eV/atom)	a = 4.04 [60] c = 5.80 [60] V = 94.67 (Å^3/cell) [60]
ω-Al_7Cu_2Fe, Tetr. I-4m2 (Nr.119)	a = 6.333 c = 14.763 V = 592.14 ΔE_{form} = −0.253	328 14.773 591.49 (Å^3/cell) −0.236 (eV/atom)	a = 6.336 [61] 6.338 [62] c = 14.870 [61] 14.832 [62] V = 597.0 (Å^3/cell) [61] 595.73 [62]

Table 2 shows that the calculated formation energy for θ-$Al_{13}Fe_4$ is more prominent than/close to the scattered experimental data. The GGA calculations provide lower formation energy for θ′-Al_2Cu than that for θ-Al_2Cu. This is against the experimental observations that the latter is the ground state [17–19]. Meanwhile, the GGA + U approximation produces a significant difference of correction effect on the formation energies of the Al_2Cu phases [50] so that θ-Al_2Cu has a lower energy than θ′-phase. Such a difference of the on-site Coulomb interaction correction originates from the local coordination of Cu in the two phases (Figure 2). The Cu atoms in θ-Al_2Cu have eight Al and two Cu neighbors, whereas the Cu atoms in θ′-Al_2Cu have only eight Al neighbors (Figure 2c,f).

To gain insight into the physics behind these results, we also performed electronic structure calculations for the three Cu-containing compounds using the GGA + U approach (Figure 3).

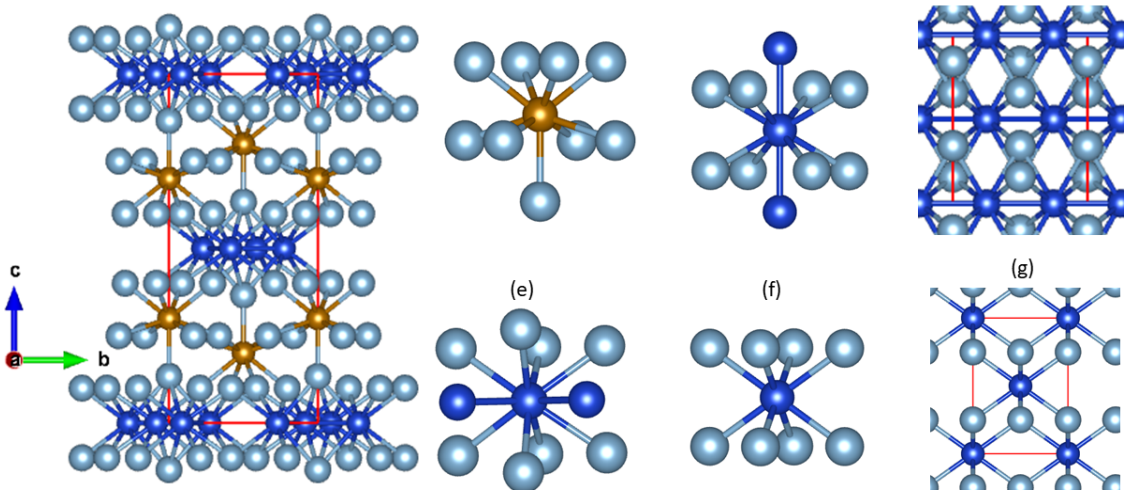

Figure 2. (Color on line) Schematic structure of ω-Al_7Cu_2Fe along its [100] direction (**a**) and related coordination of Fe (**b**) and Cu (**e**); of θ-Al_2Cu (**d**) and the coordination of Cu (**c**); and of θ′-Al_2Cu (**g**) and the coordination of Cu (**f**). The silvery spheres represent Al, the blue spheres represent Cu, and the goldish spheres represent Fe.

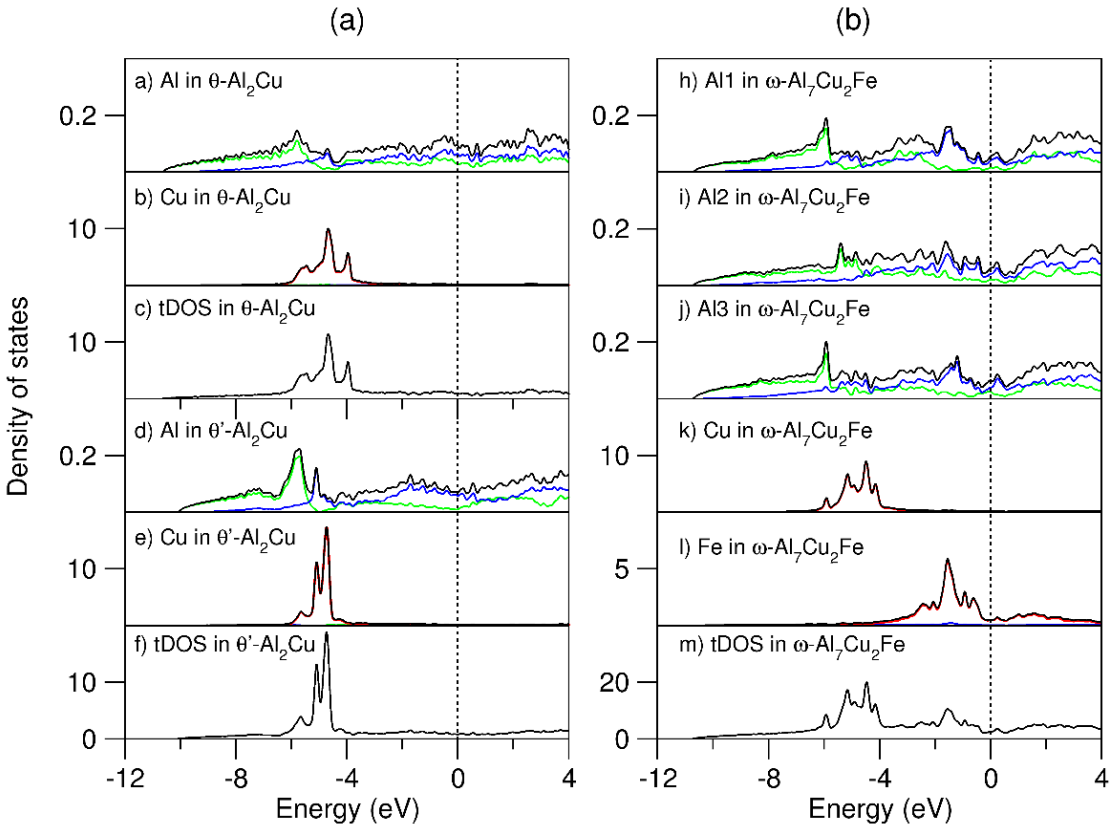

Figure 3. (Color on line) Partial and total density of states for the Al-rich Cu-containing compounds in Al-Fe-Cu system using the DFT-GGA with Hubbard U correction for Cu 3d electrons. Subfugures a) to c) for the partial density of states (pDOS) of atoms in and total density of states (tDOS) of θ-Al_2Cu, d)-f) θ′-Al_2Cu in (**a**) and h)-m) for ω-Al_7Cu_2Fe in (**b**). For partial density of states, the green curves represent s-characters, the blue curves represent p-characters, and the red curves represent d-characters. The black curves represent the total DOS. The unit for pDOS is states/eV per atom and for tDOS is states/eV per formular unit.

As shown in Figure 3a, the frames of the DOS curves for θ′- and θ-Al_2Cu phases are similar. The DOS curves for both phases are dominated by Cu 3d states. However, there are some subtle differences. (1) The DOS of θ-Al_2Cu starts at −10.7 eV, whereas for θ′-Al_2Cu, it starts at −10.1 eV. (2) At the DOS curve of θ-Al_2Cu, the Cu 3d states range from −6.2 eV to −3.2 eV with a width of 3.0 eV, whereas for θ′-Al_2Cu, the Cu 3d states range from −6.0 eV to −3.9 eV with a width of 2.1 eV. This indicates a more localized character of the Cu 3d in θ′-Al_2Cu. The broader 3d band of θ-Al_2Cu is due to the Cu-Cu interaction, as shown in Figure 2. The more localized character of the Cu 3d in θ′-Al_2Cu is the cause of the more significant on-site Coulomb interaction correction effect on the formation energy.

Figure 3b shows that the tDOS curve for ω-Al_7Cu_2Fe is primarily determined by the Cu and Fe 3d states. The tDOS starts at −10.7 eV, similar to that of θ-Al_2Cu. The Cu 3d states range from −6.2 eV to −3.1 eV with a width of 3.1 eV, which is also close to that of θ-Al_2Cu. This is understandable, since the Cu atoms have eight Al and two Cu neighbors in both structures, as shown in Figure 2. There is little direct interaction between Cu 3d electrons and those at the Fe 3d orbitals in ω-Al_7Cu_2Fe (Figure 2). This agrees with the study that Cu 3d electrons behave as a semi-core level (Section 3.1). The Fe 3d states dominate the upper part of the valence band, ranging from −3.5 eV to −0.2 eV and extend to the upper part of the valence band and the lower part of the conduction band. This relates to the more delocalized character of the unfilled Fe 3d states in such metallic systems.

3.3. Cu Substitution at the Atomic Sites in θ-$Al_{13}Fe_4$

We first define the energy of a substituted Cu at the Al and Fe sites in θ-$Al_{78}Fe_{24}$ with respect to θ-$Al_{13}Fe_4$ and elemental Cu, Al, and Fe as,

$$\Delta E_{\text{subs}}(\theta\text{-}Al_{77}CuFe_{24}) = E(\theta\text{-}Al_{77}CuFe_{24}) - [E(\theta\text{-}Al_{78}Fe_{24}) + (E(Cu) - E(Al)] \quad (3)$$

$$\Delta E_{\text{subs}}(\theta\text{-}Al_{78}CuFe_{23}) = E(\theta\text{-}Al_{78}CuFe_{23}) - [E(\theta\text{-}Al_{78}Fe_{24}) + (E(Cu) - E(Fe)] \quad (4)$$

Equation (3) is for Cu substitution of an Al, and Equation (4) is for Cu substitution of an iron in θ-$Al_{13}Fe_4$. The calculated results, including the coordination of Cu and the substitution energy, together with the local coordination in pure θ-$Al_{13}Fe_4$ as a comparison, are listed in Table 3.

The explorations reveal that Cu substitutions of Al generally do not change the local coordination. However, in the local chemical bonds for Cu at the Al sites, the Cu-Fe bond-lengths are slightly larger than the corresponding Al-Fe ones, whereas the Cu-Al bond-lengths are slightly shorter than the corresponding Al-Al bonds. Meanwhile, Cu substitutions of Fe cause longer Cu-Al bonds and shorter Cu-Fe bonds than the corresponding Fe-Al and Fe-Fe ones, respectively.

Table 3 shows that substituting one Fe with one Cu costs high energy (>0.45 eV), being unlikely. The Cu substitution of an Al7 atom is favored with negative formation energy (−0.123 eV/Cu), whereas the rest of the Cu substitutions of Al atoms cost energy. The lowest cost is one Cu atom at Al9 sites with a formation energy of 0.246 eV/Cu (Table 3 and Figure 4). Interestingly, at Al7 sites, each Cu has only two iron neighbors, compared with other sites, e.g., Al4, Al8, and Al9, where each substitution Cu has four Fe neighbors. This indicates that the number of Fe neighbors plays no significant role, corresponding to the weak interaction between the semi-core Cu 3d electrons and Fe 3d states. Meanwhile, the Al7 sites have the highest local symmetry (2/m), indicating that symmetry may play a role.

We performed structural optimization and total energy calculations for more Cu substitutions at the Al sites in θ-$Al_{13}Fe_4$. The configurations with low substitution energies are shown in Figure 4.

Table 3. Results (local coordination and substitution energy according to Equations (3) and (4)) for one Cu substitution at the Al and Fe sites in θ-$Al_{13}Fe_4$ from the GGA + U (U = 4 eV for Cu 3d) approach. Coordination of the related Cu-M (M = Al or Fe) with 3.0 Å in the substituted structures and Al/Fe-M in pure θ-$Al_{13}Fe_4$ is included.

Spe., Site (sym)	Al/Fe-M in Pure θ-$Al_{13}Fe_4$	Cu-M in Doped θ-$Al_{13}Fe_4$	ΔE_{sub} (eV/Cell)
Al1, 4i (m)	Al1-7Al(2.54–2.89) -3Fe: 2.45, 2.53, 2.62	Cu-7Al(2.44–2.84) -3Fe: 2.49, 2.66, 2.79	0.637
Al2, 4i (m)	Al2-4Al(2.92–2.97) -2Fe: 2.36(×2)	Cu-4Al(2.76–2.88) -2Fe: 2.49(×2)	0.801
Al3, 4i (m)	Al3-10Al(2.71–2.96) -2Fe: 2.44, 2.52	Cu-10Al(2.64–2.85) -2Fe: 2.53, 2.62	0.448
Al4, 4i (m)	Al4-7Al(2.53–2.75) -4Fe: 2.51, 2.61(×2), 2.63	Cu-7Al(2.41–2.68) -4Fe:2.62, 2.65(×2), 2.74	0.453
Al5, 4i (m)	Al5-8Al(2.67–2.86) -2Fe: 2.41, 2.44	Cu-10Al(2.62–2.84) -2Fe: 2.50, 2.52	0.422
Al6, 4i (m)	Al6-7Al(2.56–2.86) -3Fe: 2.47, 2.48, 2.55	Cu-7Al(2.48–2.79) -3Fe: 2.52, 2.58, 2.70	0.805
Al7, 2d (2/m)	Al7-8Al(2.69–2.80) -2Fe: 2.47(×2)	Cu-8Al(2.58–2.69) -2Fe: 2.59(×2)	−0.123
Al8, 4i (m)	Al8-7Al(2.56–2.81) -4Fe: 2.47(×2), 2.61, 2.70	Cu-7Al(2.41–2.68) -4Fe:2.55(×2), 2.69, 2.77	0.646
Al9, 4i (m)	Al9-7Al(2.53–2.67) -4Fe: 2.46, 2.49(×2), 2.86	Cu-7Al(2.39–2.57) -4Fe: 2.57, 2.58(×2), 2.89	0.246
Al10, 8j (1)	Al10-9Al(2.67–2.86) -2Fe: 2.48, 2.52	Cu-9Al(2.59–2.84) -3Fe: 2.58, 2.62, 2.84	0.453
Al11, 8j (1)	Al11-9Al(2.63–2.97) -3Fe: 2.46, 2.51, 2.77	Cu-9Al(2.54–2.82) -3Fe: 2.56, 2.62, 2.87	0.387
Al12, 8j (1)	Al12-8Al(2.64–2.96) -3Fe: 2.46, 2.56, 2.64	Cu-9Al(2.59–2.96) -3Fe: 2.55, 2.62, 2.85	0.586
Al13, 8j (1)	Al13-7Al(2.67–2.88) -3Fe: 2.44, 2.55, 2.58	Cu-8Al(2.60–2.97) -3Fe: 2.52, 2.59, 2.75	0.661
Al14, 8j (1)	Al14-8Al(2.64–2.92) -3Fe: 2.45, 2.46, 2.81	Cu-9Al(2.38–2.70)	2.074
Al15, 8j (2)	Al15-8Al(2.78–2.89) -4Fe: 2.46(×4)	Cu-8Al(2.72–2.81) -4Fe: 2.51(×4)	0.879
Fe1, 4i (m)	Fe1-11Al(2.46–2.86)	Cu-11Al(2.51–2.93)	0.548
Fe2, 4i (m)	Fe2-10Al(2.44–2.70)	Cu-10Al(2.49–2.85)	0.548
Fe3, 4i (m)	Fe3-10Al(2.44–2.77) -1Fe: 2.91	Cu-10Al(2.50–2.88) -1Fe: 2.86	0.638
Fe4, 4i (m)	Fe4-10Al(2.41–2.72) -1Fe: 2.93	Cu-10Al(2.47–2.77) -1Fe: 2.91	0.672
Fe5, 8j (1)	Al1-9Al(2.36–2.61)	Cu-9Al(2.37–2.70)	1.004

The calculations reveal that Cu substitution at the Al sites is favorable and the formation energy decreases with increasing Cu concentration, reaching the minimum when Cu fully occupies the Al7 sites. This produces a stable structural model, θ-$Al_{76}Cu_2Fe_{24}$. As shown in Figure 4, three Cu substitutions at two Al7 sites and one Al9 site has a small formation energy of +0.030 eV. This minor energy cost can be easily compensated by configuration entropy contribution at elevated temperature. Partial Si substitution of Al7 and Al9 sites produces extra freedom (number of independent configurations): w = 2 for one Si atom

at Al7 and $w = 1$ for two Si occupying the Al7 sites; $w = 2 \times 4 = 8$ for one Si at Al7 and one at Al9. For the full occupation of the Al7 sites, $w = 4$ for one extra Si, 6 for two Si, 4 for 3 Si, and 1 for four Si atoms occupying the Al9 sites. The Gibbs free energy expression is given as $\Delta G = \Delta H - T\,\Delta S_{conf}$, where $\Delta S_{conf} = k\mathrm{B} \ln w$. Here, kB is the Boltzmann's constant, and w represents the extra freedom. We calculated the Gibbs free energy for the configurations, with Si substitutions at the Al7 and Al9 sites. The obtained results are shown in Figure 4. At 1000 K, we found that the Gibbs free energy of the configuration, where two Si are at Al7 sites and one Si is at the Al4 site, is negative due to the configurational entropy contribution. Next, we focus on the crystal chemistry of θ-$Al_{76}Cu_2Fe_{24}$.

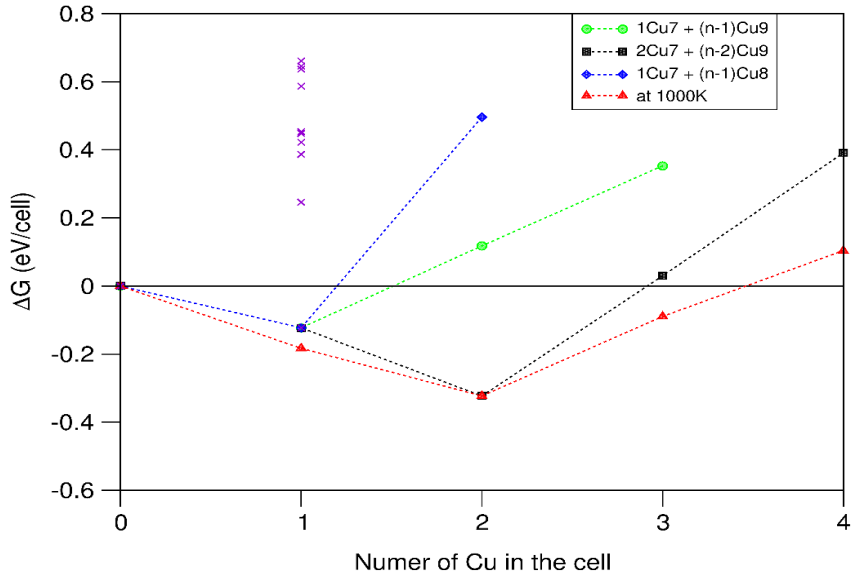

Figure 4. (Color on line) Dependence of substitution energy on Cu concentration for configurations of high stability at 0 K and related free energy at 1000 K.

3.4. Crystal and Electronic Properties of θ-$Al_{76}Cu_2Fe_{24}$

We present the results of the stable θ-$Al_{76}Cu_2Fe_{24}$ phase. The first-principles GGA + U calculations produce the lattice parameters and formation energy with respect to the elemental solids according to Equation (2). The results for θ-$Al_{76}Cu_2Fe_{24}$ and the parent θ-$Al_{78}Fe_{24}$ are shown and compared in Table 4. Figure 5 shows the schematic structure of θ-$Al_{76}Cu_2Fe_{24}$ projected along its [10] direction and the local coordination of a Cu atom.

The Cu substitution reduces the lengths of *b*-axis but increases the lengths of the *a*-axis, the *c*-axis, and the angle, β. The volume of the unit cell of the Cu substituted crystal becomes smaller, as well. With respect to the elemental solids, the ternary θ-$Al_{76}Cu_2Fe_{24}$ phase has a lower formation energy as compared to the parent θ-$Al_{78}Fe_{24}$ and the elemental Al and Cu solids.

The atomic coordinates in the ternary θ-$Al_{76}Cu_2Fe_{24}$ phase follow the same trend in that they differ slightly from the corresponding ones in the binary θ-$Al_{78}Fe_{24}$, as shown clearly in Table 4. To better compare the ternary θ-$Al_{76}Cu_2Fe_{24}$ phase with the parent θ-$Al_{78}Fe_{24}$, we performed electronic band structures for the two compositions. The partial density of states (pDOS) for the 3d transition metals and total density of states (tDOS) in the two compounds and the dispersion curves are compared in Figures 6 and 7, respectively.

For both compounds, the DOS curves have one band, starting at −10.9 eV. The upper part of the valence band from −3.0 eV to −0.2 eV is dominated by Fe 3d states, which form rather flat bands, as shown in Figure 7. The Cu 3d states form a band ranging from −5.6 eV to −2.5 eV with a peak at −4.3 eV. There are tails of the Cu 3d states at about −1.0 eV. Overall, the Cu 3d orbitals are fully occupied and contribute little to the chemical bonding in the crystal.

The frame of the dispersion curves near the Fermi level is similar (Figure 7) since they are determined by the Fe-Al interaction. Figure 7 also shows that the states along the Γ-X line (about 0.6 eV) are slightly more dispersive than those at the Γ-Y and Γ-Z lines (typically ~0.4 eV). Considering the length ratios, there is no strong anisotropy in both θ-$Al_{78}Fe_{24}$ and θ-$Al_{76}Cu_2Fe_{24}$ crystals, which is different from other Fe-IMCs, e.g., β-AlFeSi [28].

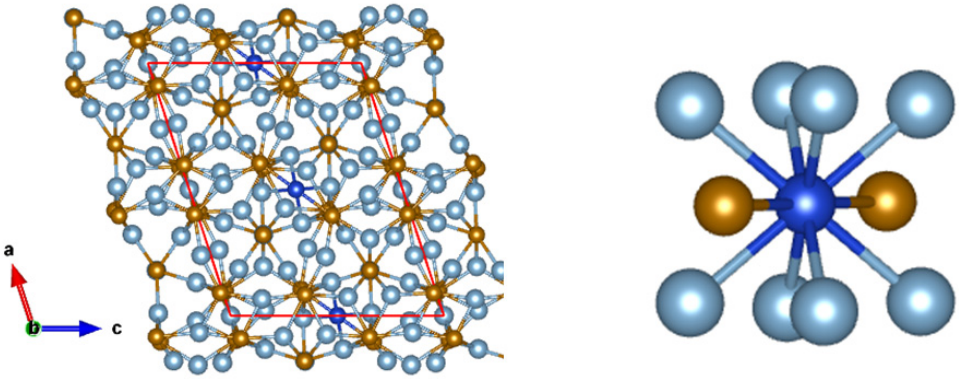

Figure 5. (Color on line) Schematic structure of the ternary θ-$Al_{76}Cu_2Fe_{24}$ phase projected along its [010] orientation and the related coordination of Cu by Fe and Al (**b**). The meaning of the spheres is the same as in Figure 2. The red lines in (**a**) represent the axis.

Table 4. The calculated lattice parameters, formation energy, and coordinates of atoms in θ-$Al_{76}Cu_2Fe_{24}$. The related results for the parent θ-$Al_{78}Fe_{24}$ are included for sake of comparison. * The Al7 sites are occupied by Cu.

Compound		**θ-$Al_{78}Fe_{24}$**			**θ-$Al_{76}Cu_2Fe_{24}$**		
Lattice Parameters (Å)		a = 15.426, b = 8.022, c = 12.425;			a = 15.504, b = 7.930, c = 12.459;		
		B = 107.68(°), V = 1464.92(Å^3)			B = 108.16 (°), V = 1455.62(Å^3)		
ΔE_{form} (eV/atom)		−0.329			−0.332		
Species	site	x	y	z	x	y	z
Al1	4i	0.065	0	0.173	0.066	0	0.1727
Al2	4i	0.323	0	0.2812	0.3214	0	0.2786
Al3	4i	0.2371	0	0.5354	0.2334	0	0.5362
Al4	4i	0.0737	0	0.5803	0.0738	0	0.5794
Al5	4i	0.2409	0	0.9613	0.2391	0	0.9557
Al6	4i	0.4788	0	0.83	0.4778	0	0.8312
Al7	2d	0.5	0	0.5	0.5	0	0.5000 *
Al8	4i	0.3049	0	0.7726	0.305	0	0.7715
Al9	4i	0.0874	0	0.7883	0.0826	0	0.7845
Al10	8j	0.1854	0.2175	0.1107	0.1859	0.2166	0.1108
Al11	8j	0.368	0.2117	0.1097	0.3682	0.2111	0.1102
Al12	8j	0.1782	0.2193	0.3345	0.1787	0.2187	0.3366
Al13	8j	0.4922	0.2333	0.33	0.4901	0.2222	0.3352
Al14	8j	0.3631	0.2186	0.4781	0.367	0.2064	0.4768
Al15	4g	0	0.2503	0	0	0.2501	0
Fe1	4i	0.0853	0	0.383	0.0836	0	0.3812
Fe2	4i	0.4015	0	0.6237	0.396	0	0.6298
Fe3	4i	0.0908	0	0.9878	0.0904	0	0.9872
Fe4	4i	0.402	0	0.9851	0.4022	0	0.9861
Fe5	8j	0.3198	0.2935	0.2779	0.3205	0.2942	0.2774

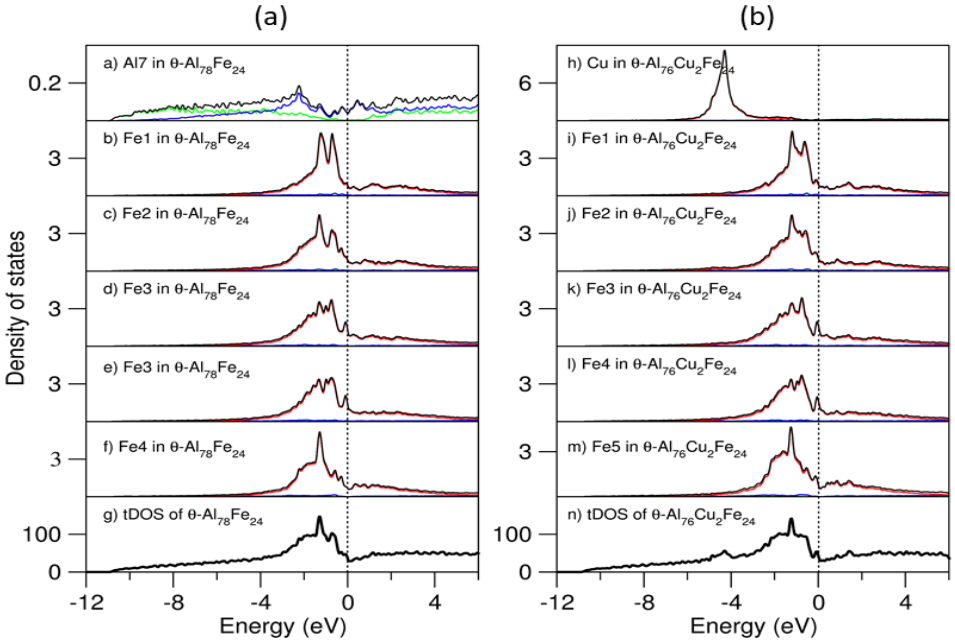

Figure 6. (Color on line) The pDOS of the selected atoms and tDOS curves for the binary θ-$Al_{78}Fe_{24}$ (**a**) and the θ-$Al_{76}Cu_2Fe_{24}$ phase (**b**). For the pDOS, a) to f) and h) to m), the green curves represent contributions from the s-character states, blue the p-character, red the d-character and black the sum of the s, p and d states of the atoms.

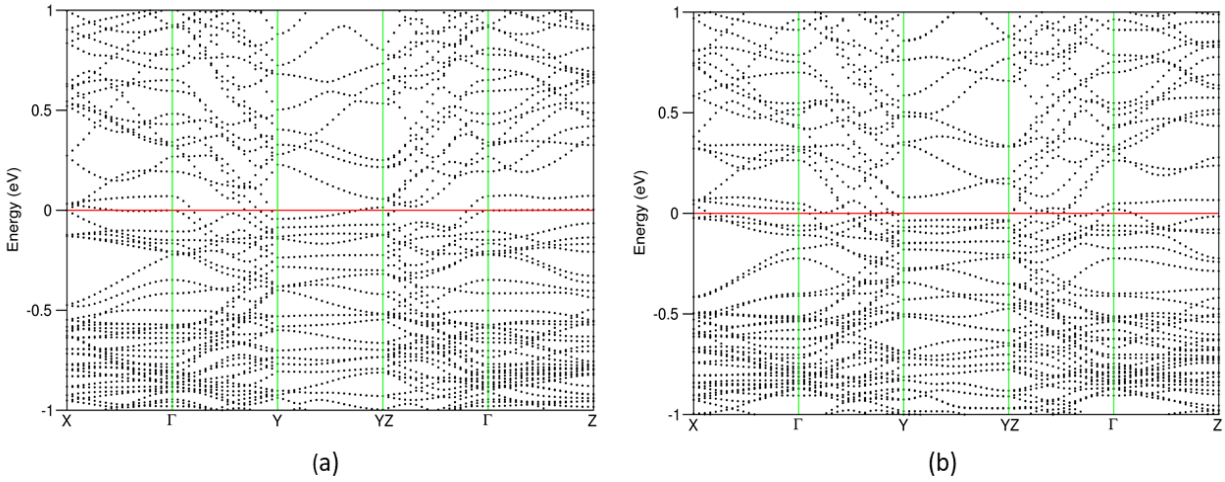

Figure 7. (Color on line) Dispersion curves of states around the Fermi level along the main axis for θ-$Al_{78}Fe_{24}$ (**a**) and for θ-$Al_{76}Cu_2Fe_{24}$ phase (**b**). The red lines represent the Fermi level (at 0 eV).

4. Discussion

First, we discuss the importance of the on-site Coulomb correction for metallic compounds containing narrow bands, e.g., Cu 3d. The DFT + U correction has been used to describe Cu-containing inorganic compounds, e.g., oxides [48,49]. Recently, our work has shown that it is also essential for metallic compounds containing Cu [50]. In this paper, we further describe this effect in detail. The Cu 3d states are fully occupied in the element Cu and Cu-containing metallic compounds. However, the standard DFT approximations have the Cu 3d states too close to the Fermi level, thus producing a physically meaningless interaction between Cu 3d and other metals. The Hubbard U correction pushes the Cu 3d orbitals to lower energy and thus avoids the unphysical interaction. Our calculations also showed a narrower band width of Cu 3d in θ′-Al_2Cu (2.1 eV) as compared to that in θ-Al_2Cu (3.0 eV) and in the pure Cu (~3.6 eV). Consequently, the Hubbard U correction is

more pronounced for θ′-Al_2Cu, which results in the correct prediction of stability of the Al_2Cu phases.

The calculations predicted the stable Al-rich compounds in the Al-Fe-Cu system: θ-$Al_{13}Fe_4$ in the binary Al-Fe line, θ-$Al_{76}Cu_2Fe_{24}$ in Cu-poor conditions, ω-Al_7Cu_2Fe in Cu-rich conditions, and θ-Al_2Cu in the Al-Cu line. This is in line with the thermodynamics assessments in the Al-rich phase diagrams [11–13,17–19]. In the Al-Fe-Cu system, the stable Al-rich compounds (with Cu concentrations larger than 0) are θ-$Al_{76}Cu_2Fe_{24}$, ω-Al_7Cu_2Fe, and θ-Al_2Cu. We can also find the composition relation: ω-Al_7Cu_2Fe = 1/24($Al_{76}Cu_2Fe_{24}$) + (11.5/3)(θ-Al_2Cu). Using the calculated total valence electron energies, we obtained the energy difference $\Delta E = E(\omega\text{-}Al_7Cu_2Fe) - [(1/24)\ E(Al_{76}Cu_2Fe_{24}) + (11.5/3)\ E(\theta\text{-}Al_2Cu)] = -0.234$ eV/f.u. (formula unit), and ω-Al_7Cu_2Fe is favored, in agreement with the experimental observations [17–19].

The calculations showed that θ-$Al_{76}Cu_2Fe_{24}$ is the ground state compound at low temperature. In this compound, the Cu content is 1.96 at %, in line with the phase diagrams [17–19]. However, additional Cu substitutions at the Al9 sites cost a moderate amount of energy. Partial occupation of the Al sites induces extra freedom (configurational entropy contribution in thermodynamics). At 1000 K, an additional Cu at Al9 sites is favored, forming θ-$Al_{75}Cu_3Fe_{24}$ with about 2.94 at % Cu. At 1360 K, two additional Cu can be doped into the Al9 sites, forming the θ-$Al_{74}Cu_4Fe_{24}$ structure with 3.92 at % Cu. This is close to the experimental observation by Freiburg and Grushko, who found Cu at both Al7 and Al9 sites [25], and the thermodynamics studies [17–19]. However, our calculations are different from the experimental observation of quenched samples in [26]. We believe that the quenched samples in [26] may contain impurities such as Si from the vessel, as our previous work showed that Si atoms can be doped into θ-$Al_{13}Fe_4$ [37], which in turn increases Cu solution content. This topic deserves further investigation.

5. Summary

Using the first-principles DFT approach with on-site Coulomb interaction correction, we investigated the stability, phase relations, structural properties, and electronic properties of the Al-rich compounds, θ-$Al_{13}Fe_4$, and Al_2Cu phases, ω-Al_7Cu_2Fe, as well as Cu substitution in θ-$Al_{13}Fe_4$. Due to the more localized nature of the Cu 3d electrons in θ′-Al_2Cu, the current approach predicted the θ-phase being more stable. We also found that Cu substitution at the Fe sites is too costly and thus unlikely. At ambient conditions, Cu prefers the Al7 sites, forming θ-$Al_{76}Cu_2Fe_{24}$. At a high temperature, Cu occupies the Al7 sites and partial Al9 sites, forming θ-$Al_{76-x}Cu_{2+x}Fe_{24}$. This agrees with the experimental observations. Electronic structure calculations also showed moderate contributions of the Cu 3d states to the electronic properties and chemical bonding in the Cu-containing metallic compounds.

Author Contributions: Conceptualization, C.F.; methodology, C.F.; formal analysis, C.F.; investigation, C.F.; data curation, C.F.; writing—original draft preparation, C.F.; writing—review and editing, C.F., M.S., Z.Q. and Z.F.; visualization, C.F.; supervision, Z.F.; project administration, Z.F. and Z.Q.; funding acquisition, Z.F. All authors have read and agreed to the published version of the manuscript.

Funding: This research was funded by EPSRC (UK) under grant numbers EP/N007638/1 and EP/S005102/1.

Data Availability Statement: Data is contained within the article.

Conflicts of Interest: The authors declare no conflict of interest.

References

1. Mondolfo, L.F. *Aluminium Alloys: Structure and Properties*; Butterworth & Co., Ltd.: London, UK, 1976.
2. Zhang, L.F.; Gao, J.W.; Nana, L.; Damoah, W.; Robertson, D.G. Removal of iron aluminum: A review. *Miner. Process. Extr. Metall. Rev.* **2012**, *33*, 99–157. [CrossRef]
3. Que, Z.P.; Wang, Y.; Fan, Z. Formation of the Fe-containing intermetallic compounds during solidification of Al-5Mg-2Si-0.7Mn-1.1Fe alloy. *Metal. Mater. Trans. A* **2018**, *49*, 2173–2181. [CrossRef]

4. Que, Z.P.; Mendis, C.L. Formation of theta-$Al_{13}Fe_4$ and the multi-step phase transformation to lapha-Al_8Fe_2Si, beta-Al_5FeSi and delta-Al_4FeSi_2 in Al-20Si-0l7Fe alloy. *Intermetallics* **2020**, *127*, 106960. [CrossRef]
5. Cai, Q.; Mendis, C.L.; Wang, S.A.; Chang, I.T.H.; Fan, Z. Effect of heat treatment on microstructure and tensile properties of die-cast Al-Cu-Si-Mg alloys. *J. Alloys Compd.* **2021**, *881*, 160559. [CrossRef]
6. Barbaux, Y.; Pons, G. New rapidly solidified aluminium alloys for elevated temperature applications on aerospace structures. *J. Phys. IV* **1993**, *3*, 191–196. [CrossRef]
7. Guinier, A.; Preston, G.D. Structure of age-hardened aluminium-copper alloys. *Nature* **1938**, *142*, 569–570. [CrossRef]
8. Schlesinger, M.E. *Aluminum Recycling*; Taylor & Francis Group: Abingdon-on-Thames, UK, 2017.
9. Gesing, A.; Berry, L.; Dalton, R.; Wolanski, R. Assuring continued recyclability of automotive aluminum alloys: Grouping of wrought alloys by color, X-ray adsorption and chemical composition-based sorting. In *Automotive Alloys and Aluminum Sheet and Plate Rolling and Finishing Technology Symposia, Proceedings of the TMS 2002 Annual Meeting and Exibition, Seattle, WA, USA, 18–21 February 2002*; Minerals, Metals and Materials Society (TMS): Warrendale, PA, USA; pp. 3–17.
10. Fang, X.; Shao, G.; Liu, Y.Q.; Fan, Z. Effects of intensive forced melt convection on the mechanical properties of Fe-containing Al-Si based alloys. *Mater. Sci. Eng. A* **2007**, *445*, 65–72. [CrossRef]
11. Sundman, B.; Ohnuma, I.; Dupin, N.; Kattner, U.R.; Fries, S.G. An assessment of the entire Al-Fe system including D0(3) ordering. *Acta Mater.* **2009**, *57*, 2896–2908. [CrossRef]
12. Zienert, T.; Fabrichnaya, O. Experimental investigation and thermodynamic assessment of the Al-Fe system. *J. Alloys Compd.* **2018**, *743*, 795–811. [CrossRef]
13. Li, X.L.; Scherf, A.; Heilmaier, M.; Stein, F. The Al-rich part of the Fe-Al phase diagram. *JPEDAV* **2016**, *37*, 162–173. [CrossRef]
14. Shabestari, S.G. The effect of iron and manganese on the formation of intermetallic compounds in aluminum-silicon alloys. *Mater. Sci. Eng. A* **2004**, *383*, 289–298. [CrossRef]
15. Malakhov, D.V.; Panahi, D.; Gallernault, M. On the formation of metallics in rapidly solidifying Al-Fe-Si alloys. *CALPHAD* **2010**, *34*, 159–166. [CrossRef]
16. Taylor, J.A. Iron-containing intermetallic phases in Al-Si based casting alloys. *Procedia Mater. Sci.* **2012**, *1*, 19–33. [CrossRef]
17. Raghavan, V. Al-Cu-Fe. *JPEDAV* **2010**, *31*, 449–452. [CrossRef]
18. Mehta, U.; Yadav, S.K.; Koirala, I.; Adhikari, D. Thermo-physical properties of ternary Al-Cu-Fe alloy in liquid state. *Philos. Mag.* **2020**, *100*, 2417–2435. [CrossRef]
19. Zhu, L.L.; Sato-Medina, S.; Cuadrado-Castillo, W.; Henning, R.G.; Manual, M.V. New experimental studies on the phase diagram of the Al-Cu-Fe quasicrystal-forming system. *Mater. Des.* **2019**, *185*, 108186. [CrossRef]
20. Corby, R.N.; Black, P.J. The structure of α–(AlFeSi) by anomalous-dispersion methods. *Acta Cryst. B* **1977**, *33*, 3468–3475. [CrossRef]
21. Cooper, M. The crystal structure of ternary alpha-(Al Fe Si). *Acta Cryst.* **1967**, *23*, 1106–1107. [CrossRef]
22. Grin, Y.; Burkhard, U.; Ellner, M.; Peters, K. Refinement of the Fe_4Al_{13} structure and its relationship to the quasihomogical homeotypical structures. *Z. Krist.* **1994**, *209*, 479–487.
23. Popčević, P.; Smontara, A.; Ivkov, J.; Wencka, M.; Komelj, M.; Jeglič, P.; Vrtnik, S.; Bohnar, M.; Jagličić, Z.; Baer, B.; et al. Anisotropic physical properties of the $Al_{13}Fe_4$ complex intermetallic and its ternary derivative $Al_{13}(Fe, Ni)_4$. *Phys. Rev. B* **2010**, *81*, 184203. [CrossRef]
24. Jeglič, C.; Vrtnik, S.; Bobnar, M.; Klanjček, M.; Bauer, B.; Gille, P.; Grin, Y.; Haarmann, F.; Dolinček, J. M-Al-M groups trapped in cages of $Al_{13}M_4$ (M = Co, Fe, Ni, Ru) complex intermetallic phases as seen via NMR. *Phys. Rev. B* **2010**, *82*, 104201. [CrossRef]
25. Freiburg, C.; Grushko, B. An $Al_{13}Fe_4$ phase in the Al-Cu-Fe alloy system. *J. Alloys Compd.* **1994**, *210*, 149–152. [CrossRef]
26. Genba, M.; Sugiyama, K.; Hiraga, K.; Yokoyama, Y. Crystalline structure of a Cu-substituted λ-$Al_{13}Fe_4$ phase by means of the anomalous X-ray scattering. *J. Alloys Compd.* **2002**, *342*, 143–147. [CrossRef]
27. Wang, J.; Shang, S.L.; Wang, Y.; Mei, Z.G.; Liang, Y.F.; Du, Y.; Liu, Z.K. First-principles calculations of binary compounds: Enthalpies of formation and elastic properties. *CALPHAD* **2011**, *35*, 562–573. [CrossRef]
28. Fang, C.M.; Que, Z.P.; Fan, Z. Crystal Chemistry and Electronic Structure of the β-AlFeSi phase from First-Principles. *J. Solid State Chem.* **2021**, *299*, 122199. [CrossRef]
29. Staab, T.E.M.; Folegati, P.; Wolfertz, I.; Puska, M.J. Stability of Cu-precipitates in Al-Cu alloys. *Appl. Sci.* **2018**, *8*, 1003. [CrossRef]
30. Janthon, P.; Luo, S.J.; Kozlov, S.M.; Viñes, F.; Limtrakul, J.; Truhlar, D.G.; Illas, F. Bulk properties of transition metals: A challenge for the design of universal density functional. *J. Chem. Theory Comput.* **2014**, *10*, 3832–3839. [CrossRef]
31. Zienert, T.; Leineeber, A.; Fabrichnaya, O. Heat capacity of Fe-Al intermetallics: B2-FeAl, $FeAl_2$, Fe_2Al_5 and Fe_4Al_{13}. *J. Alloys Compd.* **2017**, *725*, 848–859. [CrossRef]
32. van Alboom, A.; Lemmens, B.; Breitbach, B.; de Grave, E.; Cottenier, S.; Verbeken, K. Multi-method identification and characterization of the intermetallic surface layers of Al-coated steel: $FeAl_3$ or Fe_4Al_{13} and Fe_2Al_5 or Fe_2Al_{5+x}. *Surf. Coat. Technol.* **2017**, *324*, 419–428. [CrossRef]
33. Ledieu, J.; Gaudry, E.; Loli, L.N.; Villaseca, S.A.; de Weerd, M.C.; Hahne, M.; Gille, P.; Dubois, J.M.; Fournée, V. Structural investigation of the (010) surface of the $Al_{13}Fe_4$ catalyst. *Phys. Rev. Lett.* **2013**, *110*, 076102. [CrossRef]
34. Armbrüster, M.; Kovnir, K.; Friedrich, M.; Teschner, D.; Wowsnick, G.; Hahne, M.; Gille, P.; Szentmiklósi, L.; Feuerbacher, M.; Heggen, M.; et al. $Al_{13}Fe_4$ as a low-cost alternative for palladium in heterogeneous hydrogenation. *Nat. Mater.* **2012**, *11*, 690–693. [CrossRef]

35. Fang, C.M.; Dinsdale, A.; Que, Z.P.; Fan, Z. Intrinsic defects in and electronic properties of θ-$Al_{13}Fe_4$: An ab initio DFT study. *J. Phys. Mater.* **2019**, *2*, 015004. [CrossRef]
36. Dinsdale, A.; Fang, C.M.; Que, Z.P.; Fan, Z. Understanding the thermodynamics and crystal structure of complex Fe containing intermetallic phases formed on solidification of aluminium alloys. *JOM* **2019**, *71*, 1731–1736. [CrossRef]
37. Fang, C.M.; Que, Z.P.; Dinsdale, A.; Fan, Z. Si solution in θ-$Al_{13}Fe_4$ from first-principles. *Intermetallics* **2020**, *126*, 106939. [CrossRef]
38. Kresse, G.; Hafner, J. Ab initio molecular-dynamics simulation of the liquid-metal-amorphous-semiconductor transition in germanium. *Phys. Rev. B* **1994**, *49*, 14251–14269. [CrossRef] [PubMed]
39. Kresse, G.; Furthmüller, J. Efficiency of ab-initio total energy calculations for metals and semiconductors using a plane-wave basis set. *Comput. Mater. Sci.* **1996**, *6*, 15–50. [CrossRef]
40. Blöchl, P.E. Projector augmented-wave method. *Phys. Rev. B* **1994**, *50*, 17953–17978. [CrossRef]
41. Perdew, J.P.; Burke, K.; Ernzerhof, M. Generalized gradient approximation made simple. *Phys. Rev. Lett.* **1996**, *77*, 3865–3868. [CrossRef]
42. Fang, C.M.; Sluiter, M.H.F.; van Huis, M.A.; Ande, C.K.; Zandbergen, H.W. Origin of predominance of cementite among iron carbides in steel at elevated temperature. *Phys. Rev. Lett.* **2010**, *105*, 055503. [CrossRef]
43. Monkhorst, H.J.; Pack, J.D. Special points for Brillouin-zone integrations. *Phys. Rev. B* **1976**, *13*, 5188–5192. [CrossRef]
44. Wyckoff, R.W.G. *The Structure of Crystals*; Reinhold Publishing Corporation: New York, NY, USA, 1963.
45. Arblaster, J. *Selected Values of the Crystallographic Properties of the Elements*; ASM International: Materials Park, OH, USA, 2018.
46. Connelly, N.G.; Damhus, T.; Hartshorn, R.M.; Hutton, A.T. *Nomenclature of Inorganic Chemistry: IUPAC Recommendations*; RSC Publishing: Cambridge, UK, 2005.
47. Hubbard, J. Electron correlations in narrow energy bands. *Proc. R. Soc. Lond. Ser. A* **1963**, *276*, 238–257.
48. Lichtenstein, A.I.; Anisimov, V.I.; Zaanen, Z. Density-functional theory and strong interactions: Orbital ordering in Mott-Hubbard insulators. *Phys. Rev. B* **1995**, *52*, R5467. [CrossRef] [PubMed]
49. Wang, L.; Maxisch, T.; Ceder, G. Oxidation energies of transition metal oxides within the GGA + U framework. *Phys. Rev. B* **2006**, *73*, 195107. [CrossRef]
50. Souissi, M.; Fang, C.M.; Sahara, R.; Fan, Z. Formation energies of θ-Al_2Cu phase and precursor Al-Cu compounds: Importance of on-site Coulomb repulsion. *Comput. Mater. Sci.* **2021**, *194*, 110461. [CrossRef]
51. Fadley, C.S.; Shirley, D.A. Electronic densities of states from X-ray photoelectron spectroscopy. *J. Res. Natl. Bureau Stand. A* **1970**, *74*, 543–558. [CrossRef]
52. Şaşioğlu, E.; Friedrich, C.; Blügel, S. Effective Coulomb interaction in transition metals from constrained random-phase approximation. *Phys. Rev. B* **2011**, *83*, 121101. [CrossRef]
53. Kittel, C. *Introduction to Solid State Physics*, 8th ed.; John Wiley & Sons, Inc.: Hoboken, NJ, USA, 2005.
54. Ambrosetti, A.; Silvestrelli, P.L. Cohesive properties of noble metals by van der Waals-corrected density functional theory: Au, Ag, and Cu as case studies. *Phys. Rev. B* **2016**, *94*, 045124. [CrossRef]
55. Heyd, J.; Scuseria, G.E.; Ernzerhof, M. Hybrid functionals based on a screened Coulomb potential. *J. Chem. Phys.* **2003**, *118*, 8207–8215. [CrossRef]
56. Paier, J.; Marsman, M.; Hummer, K.; Kresse, G.; Gerber, I.C.; Angyan, J.G. Screened hybrid density functionals applied to solids. *J. Chem. Phys.* **2006**, *124*, 154709. [CrossRef]
57. Bradley, A.J.; Jones, P. An X-ray investigation of the copper-aliminium alloys. *J. Inst. Met.* **1933**, *625*, 131–162.
58. Havinga, E.E.; Damsma, H.; Hokkeling, P. Compounds and pseudo-binary alloys with the $CuAl_2(Cl_6)$-type structure. I. Preparation and X-ray results. *J. Less-Common Met.* **1972**, *27*, 169–186. [CrossRef]
59. Meetsma, A.; de Boer, J.L.; van Smaalen, S. Refinement of the crystal structure of tetragonal Al_2C. *J. Solid State Chem.* **1989**, *370*, 370–372. [CrossRef]
60. Wang, S.; Fan, C. Crystal structures of Al_2Cu revisited: Understanding existing phases and exploring other potential phases. *Metals* **2019**, *9*, 1037. [CrossRef]
61. Bown, M.; Bown, P. The structure of $FeCu_2Al_7$ and T(CoCuAl). *Acta Cryst.* **1956**, *9*, 911–914. [CrossRef]
62. Tian, J.Z.; Zhao, Y.H.; Wen, Z.Q.; Hou, H.; Han, P.D. Physical properties and Debye temperature of Al_7Cu_2Fe alloy under various pressures analyzed by first-principles. *Solid State Commun.* **2017**, *257*, 6–10. [CrossRef]